

THESIS

**A Study of Baseline Compensation
System for Stable Operation of
Gravitational-wave Telescope**

Koseki Miyo

*Department of Physics
University of Tokyo*

MMM 2020

Contents

1	Background	7
1.1	Gravitational-wave	7
1.1.1	7
1.2	Sources of Gravitational-wave	7
1.2.1	7
1.3	Interferometric Gravitational-wave detection	7
1.3.1	Detection Principle	7
1.3.2	Michelson Interferometer	8
1.3.3	Null Measurement	9
1.4	Summary of the Chapter	9
2	KAGRA	11
2.1	Overview	11
2.1.1	11
2.1.2	11
2.2	KAGRA Tunnel	11
2.2.1	Tunnel Design	11
2.2.2	Geological features	11
2.3	Main Interferometer	12
2.3.1	Overview	12
2.3.2	Main Interferometer	12
2.4	Vibration Isolation System	12
2.4.1	Overview	12
2.4.2	Type-A Suspension System	12
2.5	Summary of the Chapter	12

3	Seismic Noise	13
3.1	Theory of seismic waves	14
3.1.1	Seismic Waves	14
3.1.2	Reduction Effect in the Deep Sites	16
3.1.3	Reduction Effect of the Short Baseline	16
3.2	Seismic Noise	19
3.2.1	Cultural Noises	21
3.2.2	Natural Noises	21
3.3	Study of Seismic Noise of KAGRA Mine	23
3.3.1	Overview	23
3.3.2	Experimental Arrangement	24
3.3.3	Data Processing	25
3.3.4	Study of Long-term Seismic Noise	25
3.3.5	Study of the Differential Motion Reduction	26
3.4	Summary of the Chapter	26
4	Geophysics Interferometer (GIF)	31
4.1	Introduction	31
4.1.1	Laser Strainmeter for Geophysics	31
4.1.2	Motivation in GW detectors	31
4.2	Working Principle	31
4.2.1	Asynmetric Michelson Interferometer	31
4.2.2	Seismic Strain Response	32
4.2.3	Quadrature Phase Fringe Detection	33
4.2.4	Noise	33
4.3	Optics Design	33
4.3.1	Overview	35
4.3.2	Input Output Optics	35
4.3.3	Core Optics	36
4.3.4	Frequency Stabilized Laser	36
4.4	Data Aquisition System	36
4.4.1	Realtime Processing	36
4.4.2	36
4.5	Summary of the Chapter	36

5	Baseline Compensation System	39
5.1	Basics in Seismic Isolation	39
5.1.1	Single Pendulum	39
5.1.2	Multi-stage Pendulum	40
5.2	Active Inertial Seismic Isolation	40
5.2.1	Sensor Blending Technique	41
5.2.2	Sensor Correction Technique	43
5.2.3	Feedforward Technique	44
5.2.4	Problem in Tilt-Horizontal Coupling	46
5.3	Suspension Point Interferometer (SPI)	47
5.3.1	Basic Idea	47
5.3.2	RMS Reduction	48
5.3.3	Noise Improvement	48
5.3.4	Facilitation of Lock Acquisition	48
5.3.5	Some Difficulties	48
5.4	Baseline Compensation System	49
5.4.1	Concept	49
5.4.2	Advantage of GIF	49
5.4.3	GIF as SPI	49
5.4.4	Control Scheme	49
5.5	Summary of the Chapter	49
6	Demonstration of Arm Length Compensation Control	51
6.1	Experimental Arrangement	51
6.1.1	51
6.2	Results	51
6.2.1	51
6.3	Discussion and Summary of the Chapter	51
6.3.1	Discussion	51
6.3.2	Summary	51
7	Conclusion and Future Directions	53
7.1	Conclusion	53
7.2	Future Directions	53

Chapter 1

Background

1.1 Gravitational-wave

1.1.1 ...

1.2 Sources of Gravitational-wave

1.2.1 ...

1.3 Interferometric Gravitational-wave detection

1.3.1 Detection Principle

地上の大型重力波検出器の基本要素は Michelson 型レーザー干渉計である。プラスモードの重力波が Fig.??に示すような Michelson 型レーザー干渉計を垂直に通過する場合を考える。

1.3.2 Michelson Interferometer

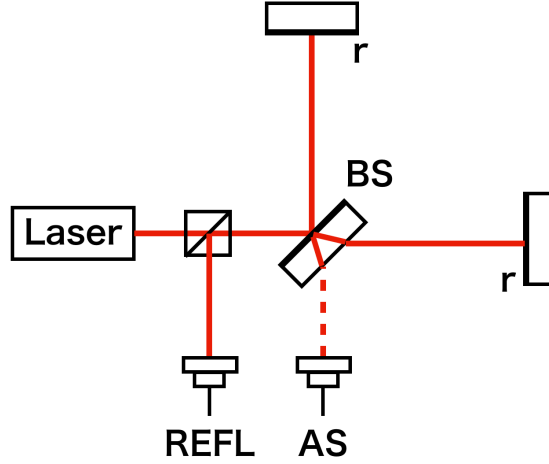


Figure 1.1: Michelson Interferometer.

Michelson interferometer is a converter from the optical phase difference of two lights to the amplitude modulation of a single light. Consider about the interferometer shown in Fig. 1.1. Incident light can be written as,

$$E_{\text{in}} = E_0 e^{i\omega t}, \quad (1.1)$$

where E_0 is the amplitude and ω_0 is the angular frequency of the laser field. Two lights split by the Beam Splitter (BS) interfere at the Anti-symmetric (AS) port and Reflection (REFL) port. The output field at the AS port is represented as,

$$E_{\text{AS}} = -\frac{1}{2}rE_0e^{i(\omega_0t-\phi_x)} + \frac{1}{2}rE_0e^{i(\omega_0t-\phi_y)}, \quad (1.2)$$

where r denotes the amplitude reflectivity of the end mirrors, and ϕ_x and ϕ_y are the phase delay due to the light traveling in the x and y arms. This output signal can be represented as a single field as,

$$E_{\text{AS}} = irE_0e^{i(\omega_0t-(\phi_x+\phi_y)/2)} \sin\left(\frac{\phi_x - \phi_y}{2}\right). \quad (1.3)$$

We find that the amplitude of the output light is a function of the difference between two phases; $\phi_x - \phi_y$. Furthermore, the power of output light at the AS port is obtained by squaring the Eq.1.3,

$$P_{\text{AS}} = (rE_0)^2 [1 - \cos(\phi_x - \phi_y)] \quad (1.4)$$

Similarly, power of the output light as REFL port is written as,

$$P_{\text{REFL}} = (rE_0)^2 [1 + \cos(\phi_x - \phi_y)]. \quad (1.5)$$

Therefore, we can measure the optical phase difference as the amplitude changes using a Photo Detector (PD) and detect GWs.

1.3.3 Null Measurement

Shot Noise

Shot noise is the optical readout noise associated with the discrete nature of photons and electric charges. 光のパワーは

Control Noise

1.4 Summary of the Chapter

Chapter 2

KAGRA

2.1 Overview

2.1.1 ...

2.1.2 ...

2.2 KAGRA Tunnel

2.2.1 Tunnel Design

KAGRA tunnel is excavated in the Kamioka mine in Hida, Gifu, Japan [1]. The tunnel is consisted of two floors. 干渉計を構成するほとんどの鏡は1階に設置された防振装置で懸架されているが、腕共振器を構成する4つの鏡は1階から14mの高さにある2階から懸架されている。

The tunnel is locate under 200 m from ground surface to decrease the seismic noise effectively.

2.2.2 Geological features

Hida region to which Kamioka belongs is a ancient region in Japan island [2].

The main bedrock is the geniss.

2.3 Main Interferometer

2.3.1 Overview

KAGRA is a cryogenic intergerometric gravitational-wave detector constructed at the underground site of Kamioka mine [3].

2.3.2 Main Interferometer

Design

The design of KAGRA interferometer is dual recycled Fabry-Perot Michelson interferometer [4][5].

2.4 Vibration Isolation System

2.4.1 Overview

KAGRA has 4 types vibration isolation system.

2.4.2 Type-A Suspension System

Type-A suspensions are developed [6].

2.5 Summary of the Chapter

Chapter 3

Seismic Noise

Seismic noise causes two issues for laser interferometric gravitational-wave detectors; (1) limitation of the low-frequency sensitivity of the detectors and (2) deterioration of the duty cycle of that. The seismic noise above 1 Hz, which is associated with anthropogenic activity, contaminates the low-frequency sensitivity. The seismic motion below this frequency, which is generated by the natural noise source such as the ocean, disturbs the Fabry-Perot arm cavity to resonate stably.

In order to resolve these issues, a laser interferometer gravitational wave antenna with a baseline length of 20 m (LISM) [7] is constructed underground, because the low-level seismic noise is expected in the underground environment. As a result, the seismic noise in LISM site is less than that in the surface site by two orders of magnitude in 1–100Hz region, and the underground GW detector performed stable operation with duty cycle of 99.8%.

However, for km-meter scale GW detector like KAGRA, such a stable operation can not be expected because

- length of the long baseline is susceptible to the low-frequency seismic motion compared with the short one due to the a few reduction effect kind of the *common mode rejection*, and this problem is common in not only all the current detectors but also the next 10 km-scale detectors; Einstein Telescope (ET)[8] and Cosmic Explorer (CE) [9].
- especially in KAGRA site, the microseismic noise correlated with the

ocean activity in 0.03–0.3 Hz, which is the most problematic noise for stable operation of GW detector, cannot be reduced even in the underground due to near the sea (40 km from Toyama Bay), and this problem is common in ET which is also will be constructed in underground but in island [10].

The purpose of this chapter is to describe quantitatively above two problems. In this chapter, first, section 3.1 gives an theoretical understanding of the seismic noise as the elastic waves. In section 3.2, some general properties of the seismic noise are described by quoting previous researches. Finally, we discuss the problems in section 3.3.

3.1 Theory of seismic waves

Here we introduce characteristics of the seismic wave that will be usefull in our later understanding and modeling of seismic effects.

3.1.1 Seismic Waves

The elastodynamic wave equation without external forces is given by

$$\rho \ddot{\mathbf{u}} = (\lambda + 2\mu) \nabla(\nabla \cdot \mathbf{u}) - \mu \nabla \times (\nabla \times \mathbf{u}), \quad (3.1)$$

where \mathbf{u} is the displacement field vector of the medium, ρ denotes density of the medium, and λ, μ are Lamé's first and second parameter.

Body Waves

From Eq.(3.1), we can obtain two characteristic waves; longitudinal wave (primary wave, P-wave) and transverse wave (secondary wave, S-wave). First, using Helmholtz's decomposition, we represent the displacement field vector \mathbf{u} as

$$\mathbf{u} = \nabla \phi + \nabla \times \boldsymbol{\psi}, \quad (3.2)$$

where ϕ the scalar potential and $\boldsymbol{\psi}$ are the vector potential. Each term of Eq.(3.2) show the divergent and the rotation component of \mathbf{u} respectively.

Substitute Eq.(3.2) into Eq.(3.1) and after some vector algebra, one can obtain two wave equations;

$$\ddot{\phi} = v_L^2 \nabla^2 \phi, \quad (3.3)$$

$$\ddot{\psi} = v_T^2 \nabla^2 \psi, \quad (3.4)$$

where v_L, v_T are defined as

$$v_L = \sqrt{\frac{\lambda + 2\mu}{\rho}}, \quad v_T = \sqrt{\frac{\mu}{\rho}}. \quad (3.5)$$

These phase velocities; v_L, v_T represent that of the P-wave and the S-wave. Show this relationships. Because the scalar potential and the vector potential are obey the wave equation Eq.(3.3) and Eq.(3.4) respectively, the general solutions of these potentials are given as

$$\phi = \phi_0(\omega t - \mathbf{k} \cdot \mathbf{x}) \quad (3.6)$$

$$\psi = \psi_0(\omega t - \mathbf{k} \cdot \mathbf{x}), \quad (3.7)$$

where ω, \mathbf{k} are the angular frequency and the wave vector. One can obtain the divergent component of displacement field vector \mathbf{u} as

$$\mathbf{u}_{\text{div}} = \nabla \phi_0(\omega t - \mathbf{k} \cdot \mathbf{x}) = -\mathbf{k} \phi. \quad (3.8)$$

The displacement of this wave \mathbf{u}_{div} whose phase velocity is v_L propagates along with direction of the wave vector. Therefore v_L is the phase velocity of a longitudinal wave called P-wave. On the other hands, one can obtain the rotation component of \mathbf{u} as

$$\mathbf{u}_{\text{rot}} = \nabla \times \psi_0(\omega t - \mathbf{k} \cdot \mathbf{x}) = -\mathbf{k} \times \psi. \quad (3.9)$$

This displacement vector \mathbf{u}_{rot} whose phase velocity is v_T is perpendicular to the wave vector. Therefore, v_T is the phase velocity of a transverse wave called S-wave. Furthermore, because λ and μ are positive numbers,

$$v_L > v_T. \quad (3.10)$$

Therefore, the longitudinal wave is faster than the transverse wave.

Rayleigh waves

Rayleigh wave は P 波と S 波の干渉によって生じる []。ここでは Z 軸を鉛直方向とした直交直線座標系の x-z 面内で振動する弾性波を考える。z=0 を自由表面とし、x 軸に沿って P 波と S 波が同じ速度 $v_R = \omega/k$ (ω is angular frequency and k is the wave vector) で伝搬する場合を考えると、ポテンシャル ϕ と ψ は、それぞれ以下のように表すことができる。

$$\phi = F(z) \exp[i(kx - \omega t)], \quad (3.11)$$

$$\psi = G(z) \exp[i(kx - \omega t)] \quad (3.12)$$

Eq.3.11 と Eq.3.11 を波動方程式 Eq.3.3, Eq.3.4 に代入すれば、レイリー波の特性方程式が導かれる；

$$\left(\frac{c_R^2}{c_S^2}\right)^3 - 8\left(\frac{c_R^2}{c_S^2}\right)^2 + 8\left(3 - \frac{2}{\gamma^2}\right)\left(\frac{c_R^2}{c_S^2}\right) - 16\left(1 - \frac{1}{\gamma^2}\right) = 0 \quad (3.13)$$

where $\gamma \equiv v_L/v_T$. In case that $0 < (\frac{c_R^2}{c_S^2}) < 1$, the velocity has physically meaningful value. According to Eq.3.13, the ratio $\frac{c_R}{c_S}$ is a function of the ratio of γ . たとえば、KAGRA と同じ山の下に建設された 100m の重力波望遠鏡 CLIO での P 波と S 波の位相速度はそれぞれ AA、BB である [11] ので、 $\gamma = 1.82$ である。したがってこのときのレイリー波の位相速度は CC である。

3.1.2 Reduction Effect in the Deep Sites

レイリー波の振幅は深さに依存しており、深いほど小さくなる。

3.1.3 Reduction Effect of the Short Baseline

For interferometric gravitational-wave detectors which need a precise length control of the optical resonate cavity, it is appropriate to consider about the relative displacement between two points rather than the displacement of single point.

Differential Motion and Common Motion

We define the motion of two points shown in Fig.(3.1) as $\mathbf{u}_1 = \mathbf{u}(t, \mathbf{x}_1)$ and $\mathbf{u}_2 = \mathbf{u}(t, \mathbf{x}_2)$, respectively. The motions of the two points can be represented

as the differential motion and the common motion. The displacement of both differential motion and common motion of the two points shown in Fig.(3.1) are defined as

$$\mathbf{u}_{\text{diff}} \equiv \frac{\mathbf{u}_1 - \mathbf{u}_2}{\sqrt{2}}, \quad (3.14)$$

$$\mathbf{u}_{\text{comm}} \equiv \frac{\mathbf{u}_1 + \mathbf{u}_2}{\sqrt{2}} \quad (3.15)$$

These two motions defined in Eq.(3.14) and Eq.(3.15) are normalized by $\sqrt{2}$ to conserve the total power.

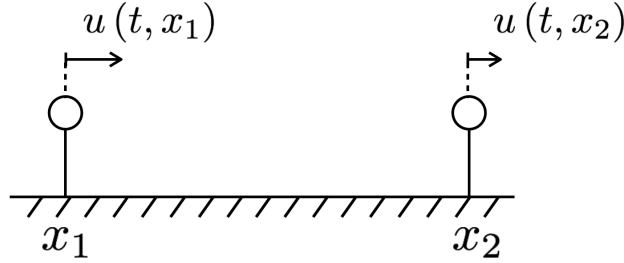


Figure 3.1: The displacements of the two points which are separated L in X axis. $\mathbf{u}(t, \mathbf{x})$ is the displacement field vector, where t denotes the time and \mathbf{x} denotes the location vector.

Common and Differential Motion Ratio (CDMR)

We define the power ratio of the common motion over the differential motion as common and differential motion ratio (CDMR). This ratio is useful to describe how the differential motion is reduced in the baseline compared to the common motion. CDMR is defined as

$$\text{CDMR} \equiv \sqrt{\frac{\text{Common Motion}}{\text{Differential Motion}}} = \sqrt{\frac{P_{\text{comm}}(\omega)}{P_{\text{diff}}(\omega)}} \quad (3.16)$$

where P_{comm} , P_{diff} are the power spectral densities (PSDs) of the differential motion and common motion, respectively. In order to obtain these PSDs, we

convert from the autocorrelation function of these. Therefore, first, autocorrelation function C_{diff} of the differential motion is given by its definition in Eq.(3.15)

$$C_{\text{diff}}(\tau) = \frac{1}{2} \left\langle \left[x_1(t) - x_2(t) \right] \left[x_1(t + \tau) - x_2(t + \tau) \right] \right\rangle \quad (3.17)$$

$$= \frac{1}{2} \left[C_{11}(\tau) - C_{12}(\tau) - C_{21}(\tau) + C_{22}(\tau) \right], \quad (3.18)$$

,where C_{ij} are the autocorrelation functions of each point and defined as $C_{ij} \equiv \langle x_i(t)x_j(t + \tau) \rangle$, ($i = 1, 2, j = 1, 2$). Here, one can obtain the power spectrum density of differential motion $P_{\text{diff}}(\omega)$ as

$$P_{\text{diff}}(\omega) = \frac{1}{2} \left[P_1(\omega) + P_2(\omega) - P_{12}(\omega) - P_{12}^*(\omega) \right] \quad (3.19)$$

$$= \frac{1}{2} \left[P_1 + P_2 - \text{Re}[\gamma] \times 2\sqrt{P_1 P_2} \right], \quad (3.20)$$

where $P_1(\omega), P_2(\omega)$ are the power spectrum densities of each points, and $P_{12}(\omega)$ are the cross spectrum between two point. The parameter γ is the complex coherence between them defined by

$$\gamma \equiv \frac{P_{12}}{\sqrt{P_1 P_2}}. \quad (3.21)$$

Furthermore, assuming that seismic wave propagating each points does not decay, which means $P_1 = P_2 \equiv P$, one can compute the $P_{\text{diff}}(\omega)$ as

$$P_{\text{diff}}(\omega) = P(1 - \text{Re}[\gamma]). \quad (3.22)$$

Similarly, the PSD of the common motion can be calculated as

$$P_{\text{comm}}(\omega) = P(1 + \text{Re}[\gamma]). \quad (3.23)$$

Finally, CDMR defined Eq.(3.16) in case the seismic wave does not decay is represented as

$$\text{CDMR} = \sqrt{\frac{1 + \text{Re}[\gamma]}{1 - \text{Re}[\gamma]}}. \quad (3.24)$$

Eq.(3.24) indicates that CDMR can be expressed by only the coherence γ between of two points. For example, CDMR tends to be larger when γ close to 1. This means that the differential motion is more less than the common motion because the two points move together in the same direction.

Uniform Plane Wave Model

Consider the CDMR when the plane waves are distributed uniformly around the azimuth. Because the coherence that the single plane wave propagating with the azimuth angle θ along the direction of arm cavity from x_1 to x_2 in Fig.(3.1) is

$$\gamma = e^{i\frac{L\cos\theta\omega}{c}}, \quad (3.25)$$

the coherence in case that the plane waves propagats uniformly is given by the integral of Eq.(3.25) over all direction;

$$\gamma = \frac{1}{2\pi} \int_{-\pi}^{\pi} e^{i\frac{\omega}{c}L\cos\theta} d\theta. \quad (3.26)$$

where the coherence is normized azimuth angle. Therefore, the CDMR is given as

$$\text{CDMR} = \sqrt{\frac{1 + J_0(\frac{L\omega}{c})}{1 - J_0(\frac{L\omega}{c})}}. \quad (3.27)$$

For later discussion in 3.3.5, the PSD of the differential motion in case of the uniform seismic waves is usefull and is given as

$$P_{\text{diff}}(\omega) = P \left[1 - J_0 \left(\frac{L\omega}{c} \right) \right]. \quad (3.28)$$

3.2 Seismic Noise

Here we describe the actual seismic noise. Characteristics of the seismic noise are related with its origin spatially and temporally. The noise sources are spreaded anywhere; foot steps, traffics and ocean waves, and these amplitude depends on day-night or weather condition.

As summarized in Table 3.2, the seismic noises above 1 Hz are cleary correlated with cultural activities, and that below this frequency are excited by the natural phenomena [12].

This boundary frequency between cultural or natural is depends on the soil structure. At the sediment site such as the LIGO[13] and Virgo site[14], the cultural noise can be shifted to a lower frequency and appear below 1 Hz. On the other hands, at the hard rock site such as KAGRA site, the cultural

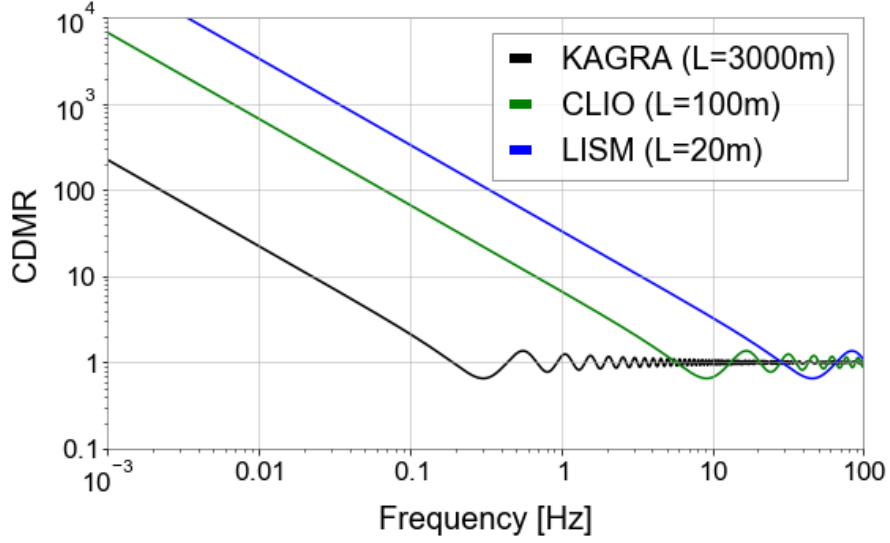


Figure 3.2: CDMR, which is the power ratio of the common motion over the differential motion of baseline in Eq.(3.27), of the underground GW detectors assuming the uniform plane waves model with phase velocity of 3000 m/sec. Black is KAGRA with the 3000 m baseline, green is CLIO with the 100 m baseline, and blue is LISM with the 20 m baseline. The CDMR of the long baseline is worse than that of short baseline. For example, at 0.1 Hz, if the baseline length is longer, the CDMR is larger..

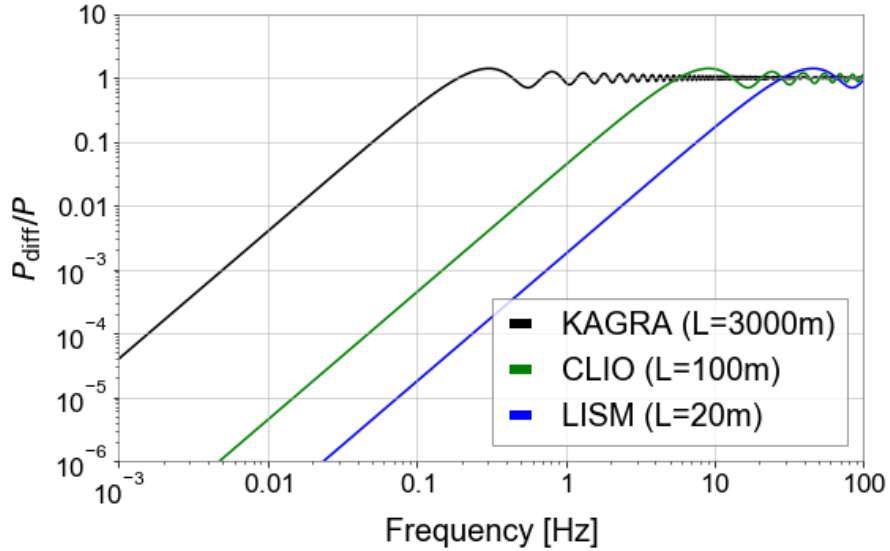


Figure 3.3: The power ratio of the differential motion of the baseline over the motion at single point; P_{diff}/P of Eq.(3.28). This ratio gives the estimation of the PSD of baseline length fluctuation from the

Table 3.1: Two types of seismic noise

Type of noise	Frequency Band	Sources
Cultural Noise	> 1 Hz	wind, traffic, machinaries, foot steps
Natural Noise	< 1 Hz	ocean, air pressure, earth tides

noise can be distinguished from the natural noise for its diurnal variability and apparent only above 1 Hz.

3.2.1 Cultural Noises

The cultural seismic noise contaminates the sensitivity of gravitational-wave detectors in the frequency range of interest for gravitational-waves sources, above 1 Hz. In this frequency band, the cultural noise is dominated by winds or human activities. For example, seismic noise from traffic near the detectors is reported at LIGO site [15], and noise from the vibrations of building excited by winds is reported at Virgo site [16].

3.2.2 Natural Noises

The natural seismic noise affects the stability of the GW detectors below 1 Hz because it deforms largely the ground on which mounted the detectors.

これら natural seismic noise は場所によって大きくことが知られている。Peterson らによって行われた、世界の 75 箇所の基地にある地震計の数年分のデータから得た地面振動のノイズスペクトルを Figure 3.4 に黒線で示す。200 mHz のピークは

Microseisms

Microseisms which power spectrum has peaks in 50–200 mHz are excited by oceanic waves. These seismic waves can be categorized by the generating mechanism of these [19]. First, the primary ocean microseisms are generated only in shallow waters in coastal regions. In this regions, the water wave energy can be converted directly into seismic energy either through vertical water pressure variations, or by the impacts of surf on the shores. There are

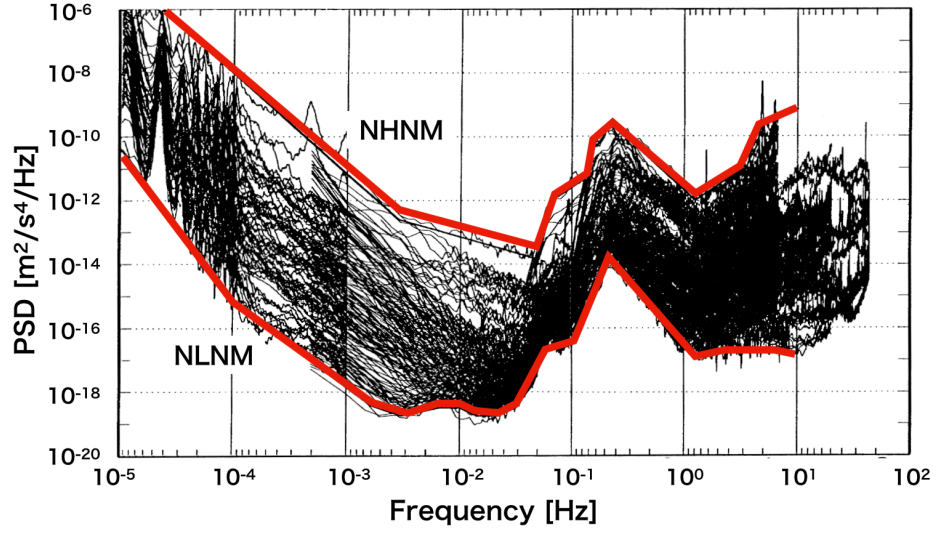


Figure 3.4: PSDs of the seismic noise obtained by Peterson in 75 stations in the world [17]. Each of the black solid lines is PSD divided into 5 different frequency band at the each stations. Each red lines are the new high noise model (NHNM) and the new low noise model (NLNM), respectively. The NHNM a spectrum of average high background noise power in the seismometer network, and the primary contributions to NHNM are inland stations situated on soft solid in very noisy locations and coastal stations with high amplitude microseisms. The NLNM represents the seismic noise when microseismic is quiet, and below microseismic, it represents the global seismic noise floor[18].

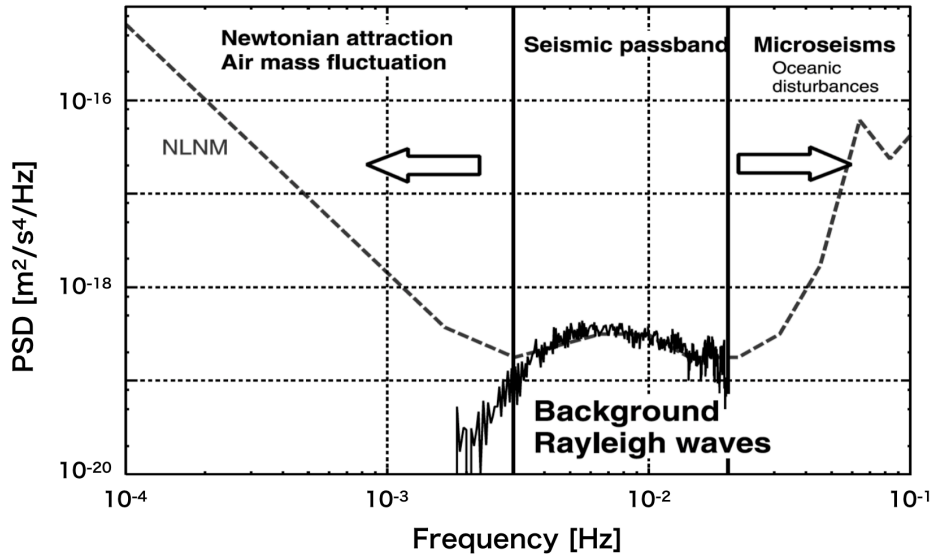


Figure 3.5: [18] から転載。

correlation between this microseismic peak and the swell at the beaches was known starting from the data sets studied by [20]. Second, the secondary ocean microseisms could be explained by the superposition of ocean waves of equal period traveling in opposite directions. Therefore, generating standing gravity waves of half the period [21].

The RMS amplitude spectral of both type of the microseisms are strongly depends on the low pressure on the ocean [10].

Seismic Noise Below 20 mHz

Below the microseismic frequency band, the main seismic noise source is an atmospheric pressure change; Rayleigh waves excited by air fluctuation on the surface, and the deformation of the Earth's crust caused by the Newtonian attraction of air mass fluctuation [22, 23]. Fig. 3.5 shows PSDs of the New Low Noise Model (NLNM) [17] and the measured former noise [18], and the noise is consistent with the NLNM between 2 Hz and 30 mHz. Moreover, the latter noise is increase PSD increases rapidly with decreasing frequency below 2 mHz. ここで特筆すべきは、2mHz 以上のノイズは Rayleigh wave で運ばれるため、地下に潜ればいくらか低減が期待されることである。実際に地表と地下のひずみ計による観測によってそれが示唆されている [24]。

Earth tides

Below more lower frequency, the earth deformed by tidal forces due to the attraction of the Sun and the Moon in diurnal and semi-diurnal period.

(なにかもう少し書く)

3.3 Study of Seismic Noise of KAGRA Mine

3.3.1 Overview

KAGRA では、我々は地面振動を地震計とひずみ計をつかったリアルタイムモニタリングシステムを構築している。このシステムの目的は、地面振動に最も敏感な腕共振器を懸架する TypeA サスペンションの地面振動をモニターすることである。そのため、我々は広帯域地震計である Trillium120 を 3 台、TypeA

が懸架されているコーナーエリアと両エンドエリアの二階の地面に設置し、ひずみ計は現在 X アームに設置している。これらセンサーは自身のセンサーノイズの特性上、帯域を相補的に地面振動をモニターしている；0.1Hz 以上は地震計で、1Hz 以下はひずみ計でモニターしている。

本節ではこれらセンサーをつかって、KAGRA の地面振動ノイズの時間的空間的な特徴を調べた。

3.3.2 Experimental Arrangement

We used Trillium 120-QA which is known as three-component, very broadband, and low-noise seismometer. These three outputs are proportional to the ground velocity of two horizontal and one vertical, respectively.



Figure 3.6: Trillium 120-QA installed on the second floor at X-end area, which is covered by black thermal insulation cover

The seismometer is housed in the black thermal insulation cover as shown in fig 3.6. Thermal insulation protects two broad categories of thermal couplings that can cause unwanted noise [25]. First is the direct coupling to the sensitivity. This coupling typically increases the noise of the vertical channel as a periodic diurnal variation caused by the day-to-night temperature cycle, because the springs that suspended the inertial masses are temperature sensitive. The second is the coupling to tilt from the thermal fluctuation. Tilt converts the vertical acceleration of gravity into horizontal acceleration. This thermally induced tilt noise on the horizontal will be larger than the

direct thermal coupling on the vertical channel. To be low sensitivity to both tilt and temperature, this model has a function to center the inertial mass after the initial installation.

The signals of the seismometer is recorded through the data acquisition system developed by LIGO [26]. The analog signal is converted to digital signal by the 16 bit analog-to-digital converters (ADC) with 16384 Hz sampling. This analog signal is amplified with 30 db so that the ADC noise does not mask this signal.

3.3.3 Data Processing

振幅スペクトルの推定は 50%オーバーラップした 32 個のセグメントの平均で得た。それぞれのセグメントの FFT の計算は、まず dtrend をして線形成分を取り除き、Hanning 窓にかけてから行った。32 回の平均をおこなったスペクトルは自由度 32 のカイ二乗分布に従う。自由度 ν のときの $100(1 - \alpha)\%$ の信頼区間は、周波数 f でのスペクトルの推定量を $\hat{G}(f)$ とすると、

$$\frac{\nu \hat{G}(f)}{\chi^2(\nu, 1 - \frac{\alpha}{2})} \leq G(f) \leq \frac{\nu \hat{G}(f)}{\chi^2(\nu, \frac{\alpha}{2})} \quad (3.29)$$

で与えられる。したがって、95%の信頼区間は

$$\nu / \chi^2(\nu, 1 - \frac{\alpha}{2}) \leq G(f) / \hat{G}(f) \leq \nu / \chi^2(\nu, \frac{\alpha}{2}) \quad (3.30)$$

となり、自由度 32 の場合、推定量の 0.65 から 1.75 の範囲になる。

3.3.4 Study of Long-term Seismic Noise

Long-term seismic noise is measured by a seismometer installed on the second floor of the X-end area. This area is placed 200 m underground from the surface of the mountain. In comparison to corner area, human activity in the end area is less because the corner area has parking lots. In comparison to the Y-end area, there is no entrance connected to other mines. Therefore, the X-end area is relatively quiet in the KAGRA mine, regarding the seismic noise induced by human activity.

地震や回路からの突発的なノイズを含まない一年間のデータをつかって、ノイズスペクトルを計算した。並進成分と垂直成分両方の加速度の ASD を

Figure 3.7 に示す。40mHz 以上では並進成分も垂直成分も同じ振幅スペクトル密度をもつ。40mHz 以下で並進成分が垂直成分よりも大きい、これは付録で後述しているとおり、無相関なノイズである。おそらく温度ゆらぎから生じる傾斜カップリングだと考えられる。また、Peterson のスペクトルと測定で得た 10 パーセンタイルを比較すると、0.1 から 2Hz をのぞいて、NLNM と同じである。0.1Hz 以下では垂直成分は地面振動のノイズレベルと同等であり。2Hz 以上は、並進も垂直成分も、地下環境のおかげで静かである。対照的に 0.1 から 2Hz の帯域では、並進成分も垂直成分も NLNM より数倍大きい。これは KAGRA が富山湾から 40km の距離にあり、比較的脈動の影響を受けやすいためと考えられる。

3.3.5 Study of the Differential Motion Reduction

CDMR in X-arm

3.1.3 でのべた CDMR の効果を, X アームの両端においた地震計 2 台をつかって評価した。

基線長の違いによる CDMR の変化

aaa

3.4 Summary of the Chapter

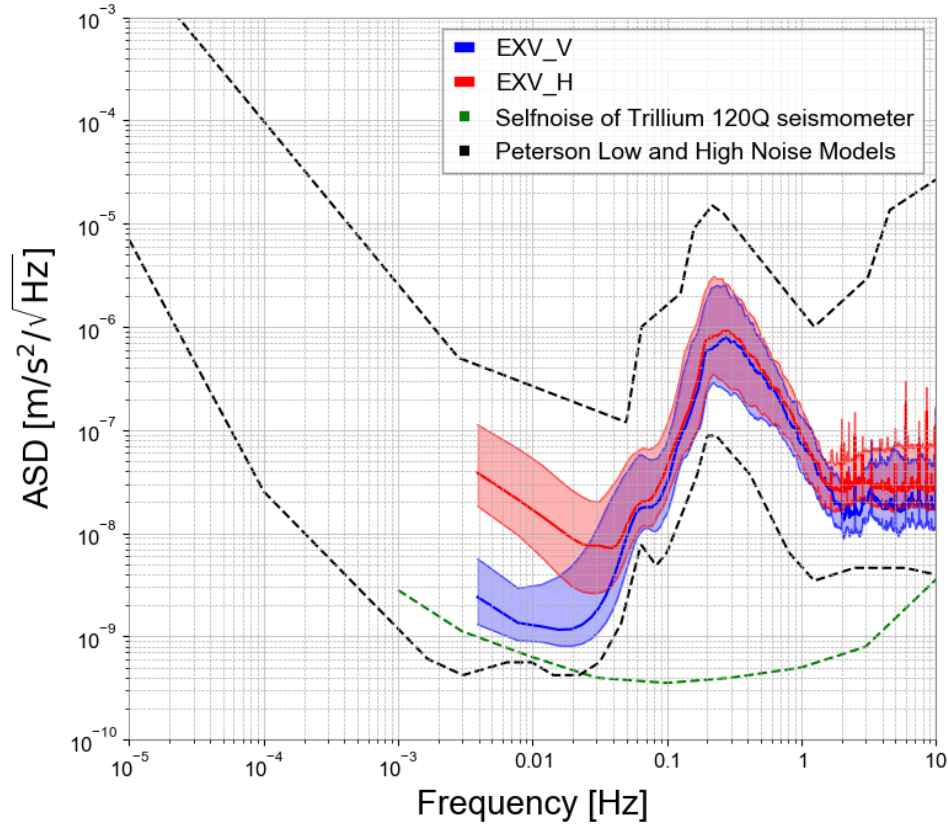


Figure 3.7: 赤の実線は垂直成分の50パーセンタイルで、下と上に10と90パーセンタイルを示す。青の実線はX軸とY軸の二乗和から求めた並進成分であり、同様に10,50,90パーセンタイルを示す。緑点線はTrillium120のデータシートから引用したSelfnoiseである。黒の点線はPetersonのNLNMとNHNMである。

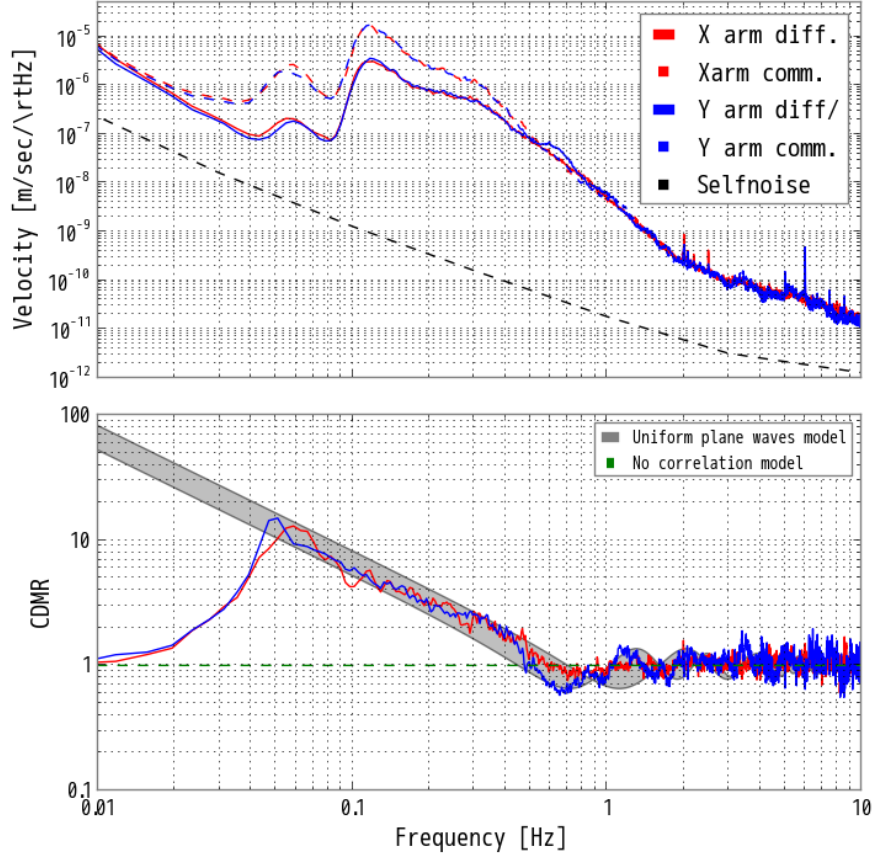
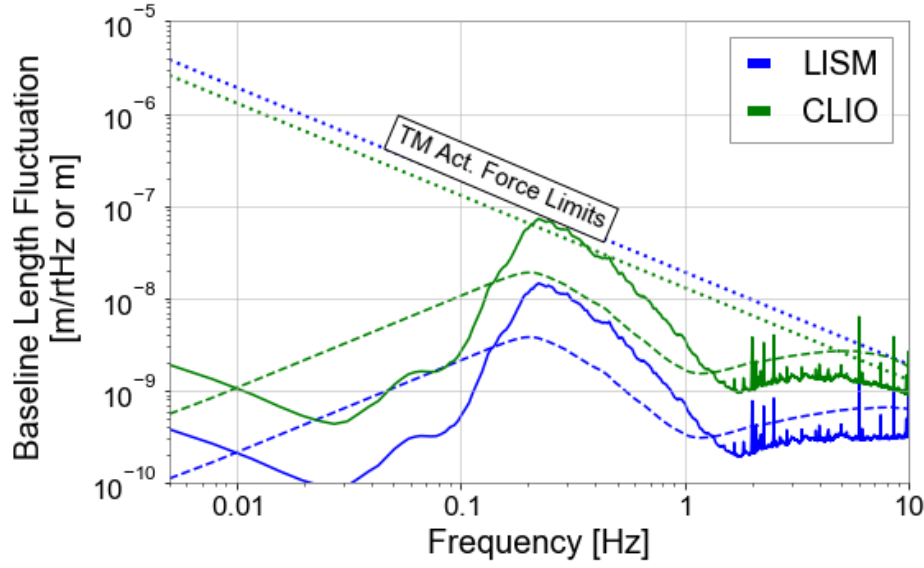
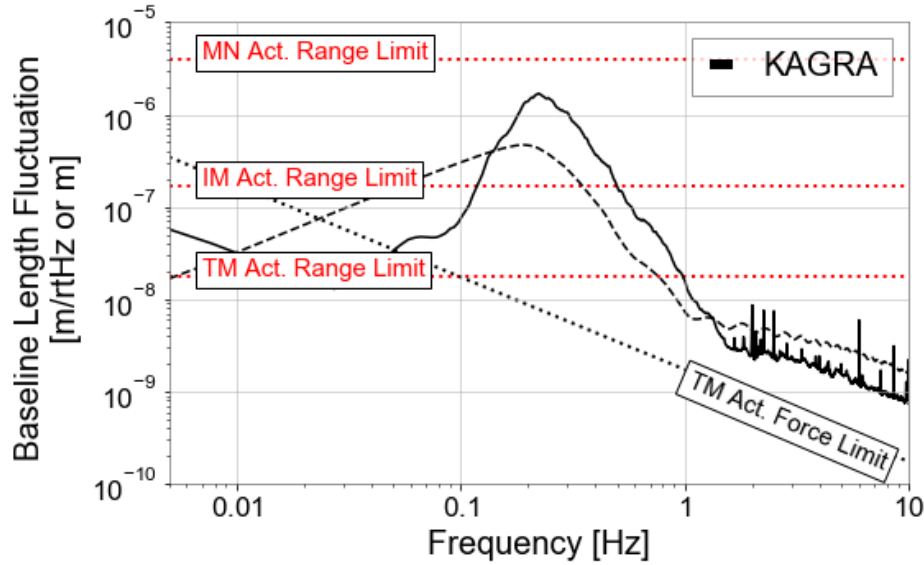


Figure 3.8: Comparison with the measured CDMR and the uniform plane waves model. (Top) ASDs of the velocity of the differential (solid line) and common motion (dashed line) of the baseline used calculating the below CDMR. Red and blue indicate X-arm and Y-arm, respectively. As a comparison to these ASDs, black dashed line shows the selfnoise of the Trillium 120Q broadband seismometer multiplied $\sqrt{2}$. Below 0.05 Hz, the ASDs are limited by the noise mentioned in section 3.3.2. (Bottom) The CDMR of the baseline calculated with the differential and common motion of the baseline according to the definition in Eq.(3.16). Gray line indicates the CDMR assuming the uniform plane waves model in case the phase velocity is in region from 5 – 3 km/sec. Green dashed line is the CDMR assuming the no correlation between the each end points of the baseline. The measured CDMR is consistent with the uniform model in 0.05 – 0.5 Hz. Below this band, the CDMR is close to the no correlation model due to the noise of the seismometers. Above this band,



(a)



- (b) Comparison between the baseline length fluctuations and the displacement requirement of the underground GW detectors. Solid line is the baseline length fluctuation of the detectors, which is the ASD of the seismic noise (described in section 3.3) multiplied by the function in Eq. ?? assuming the uniform plane wave model with the phase velocity of 3 km/sec. Moreover, dashed line is the accumulated RMS of the fluctuations. As a comparison, the displacement requirement of the detector, which is the linewidth of the arm cavity, is plotted.

Figure 3.9: aa**Table 3.2:** Comparison of the underground GW detectors

Detector	Baseline length [m]	Linewidth [μm]
LISM	20	0.1

Chapter 4

Geophysics Interferometer (GIF)

4.1 Introduction

地物干渉計の目的は、地球物理学の現象を精密に測定することと、KAGRAの基線長をモニターすることである。

4.1.1 Laser Strainmeter for Geophysics

4.1.2 Motivation in GW detectors

4.2 Working Principle

4.2.1 Asymmetric Michelson Interferometer

$$\phi = 2\pi \frac{2(l_x - l_y)}{\lambda} \sim 4\pi \frac{l_x}{\lambda} \quad (4.1)$$

$$|d\phi| = 4\pi \frac{l_x}{\lambda} \left(\left| \frac{d\lambda}{\lambda} \right| + \left| \frac{dl_x}{l_x} \right| \right) \quad (4.2)$$

4.2.2 Seismic Strain Response

In order to calculate the response from the seismic strain to the optical phase of the GIF interferometer, the same as the Fig.(3.1), it is assumed that the plane seismic waves which displacement $u(t, x)$ is represented as $u(t, x) = u_0 e^{i(\omega t - kx)}$ with angular frequency of ω and wave number of k , which propagates along with the direction of the baseline of the strainmeter (right direction in this figure). First, because the length fluctuation between two mirrors sparated with L can be expressed as

$$\Delta L(t) \equiv u(t, 0) - u(t, L) \quad (4.3)$$

$$= u(t, 0) - u(t - \tau, 0), \quad (4.4)$$

where $\tau = L/v$ is the time delay, the transfer function from the displacement to the length fluctuation is given by Laplace transform as

$$H_{\text{disp}}(s) \equiv \frac{\Delta L(s)}{u(s)} = \frac{u(s) [1 - \exp(-\tau s)]}{u(s)} = 1 - \exp(-\tau s) \quad (4.5)$$

Moreover, because the strain amplitude $\epsilon(x, t)$ is defined as $\epsilon(x, t) \equiv \frac{du}{dx}$, the seismic strain is represented as

$$\epsilon(x, t) \equiv \frac{du}{dx} = \frac{du}{dt} \frac{dt}{dx} = \frac{du}{dt} \frac{1}{v} \quad (4.6)$$

Therefore, similarly, the transfer function from the seismic strain to the displacement is given as

$$u(s) = \frac{v}{s} \epsilon(s). \quad (4.7)$$

Finary, because the transfer function from the length change of the baseline to the optical phase is given as $4\pi/\lambda_{\text{opt}}$ according to the optical gain in Eq.(4.1), the transfer function from the seismic strain to the optical phase is represented as

$$H_{\text{strain}}(s) = 4\pi \frac{1}{\lambda_{\text{opt}}} [1 - \exp(-\tau s)] \frac{v}{s}. \quad (4.8)$$

As a summary of these transfer function, these are related with each other as shown in Fig.(4.1). Furthermore, we should note the seismic strain reponse depending with the baseline length.

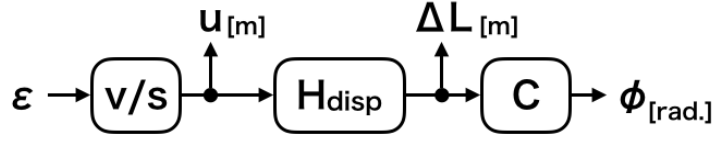


Figure 4.1: The response from seismic strain to optical phase. ϵ is the seismic strain, u is the displacement, ΔL is the length change of the X-arm baseline, and ϕ is the optical phase of the GIF interferometer. C is the optical gain of the GIF interferometer given in Eq.(4.1). H_{disp} is the transfer function from the displacement to the length change given in Eq.(4.5). v/s is the transfer function from the seismic strain to the displacement given in Eq.(4.6).

4.2.3 Quadrature Phase Fringe Detection

We use the quadrature phase fringe detection to measure the length change of the baseline with wide dynamic range [27]. The optical layout for the detection is shown in Fig.(4.3). The quadrature phase fringes are detected by two photo detectors, these can be represented as

$$x = x_0 + a \sin(p + p_0), \quad (4.9)$$

$$y = y_0 + a \sin(p), \quad (4.10)$$

where x and y are the two voltage outputs from the detectors, a and b are the amplitudes of these fringe signals, x_0 and y_0 are the offsets, and p_0 is the phase offsets from imperfections [28].

4.2.4 Noise

どういふノイズが原理的に存在するか述べる。空気ゆらぎ、周波数雑音を述べる。

4.3 Optics Design

...

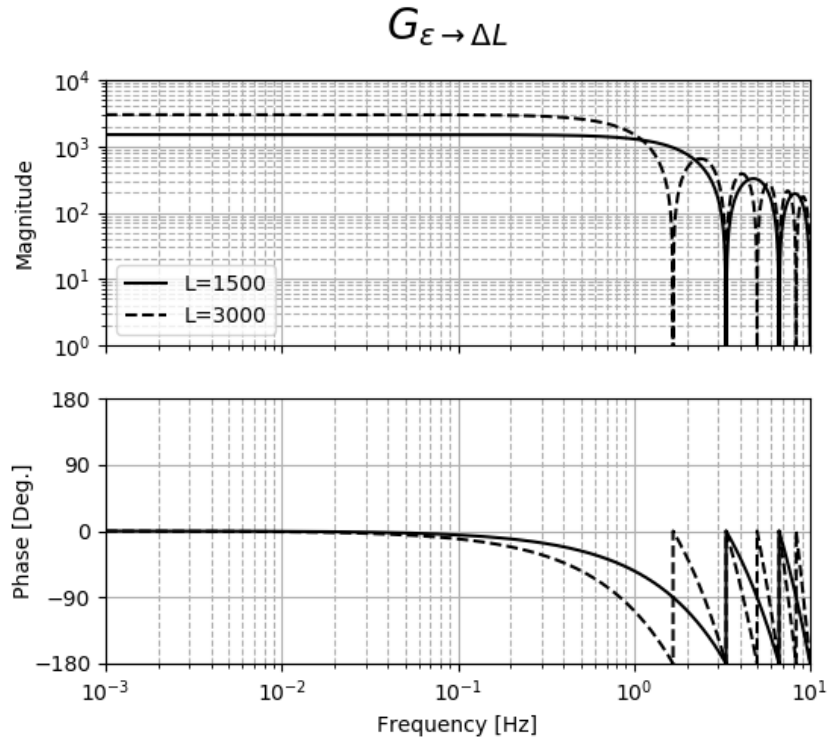


Figure 4.2: Comparison of the transfer function from strain of the baseline ϵ to the length change of that ΔL in the different baseline length. 3000 m の基線長ではその半分の 1500 Hz よりも、DC ゲインは二倍大きい一方で、コーナー周波数は A になり帯域が減る。また、周波数が B の条件を満たすとき、ゲインはゼロになる。なぜならば、このときひずみは基線を同相で動かし、基線長伸縮として現れないためである。

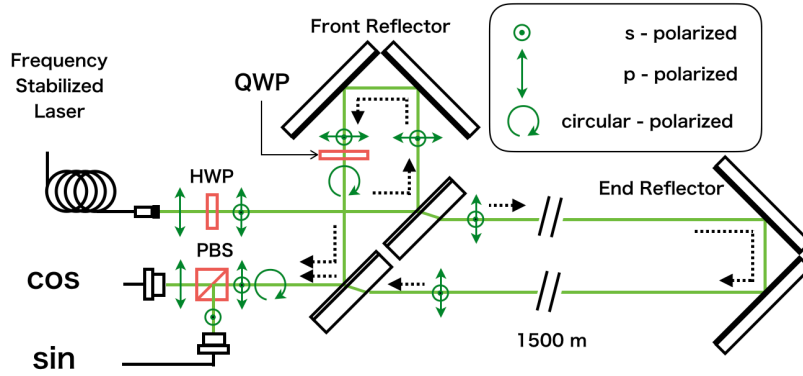


Figure 4.3: Quadrature interferometer used in the GIF strainmeter. A half-wave plate (HWP) produces a p-polarization and s-polarization. A quator-wave plate (QWP) delay the optical phase of the s-polarized light with 90 degree against to the another. As a result, one can obtain the quadrature phase fringe.

4.3.1 Overview

Optical layout is shown in Fig. ?? . Optics of GIF is categorized by three category; mode-matching optics, core optics and frequency stabilized laser.

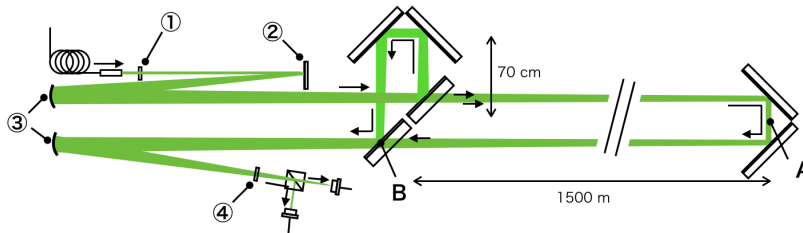


Figure 4.4: Schematic optics layout.

4.3.2 Input Output Optics

エンドリフレクタでビームウエストになるようにモードマッチさせている。

4.3.3 Core Optics

The core optics of the Michelson interferometer are composed of two reflectors and beam splitter (BS).

4.3.4 Frequency Stabilized Laser

周波数安定を行っている。

4.4 Data Aquisition System

4.4.1 Realtime Processing

4.4.2 ...

4.5 Summary of the Chapter

本章で述べたパラメータを表にまとめる。



(a) Core optics in the front vacuum chamber.



(b) Core optics in the end vacuum chamber.

Figure 4.5:

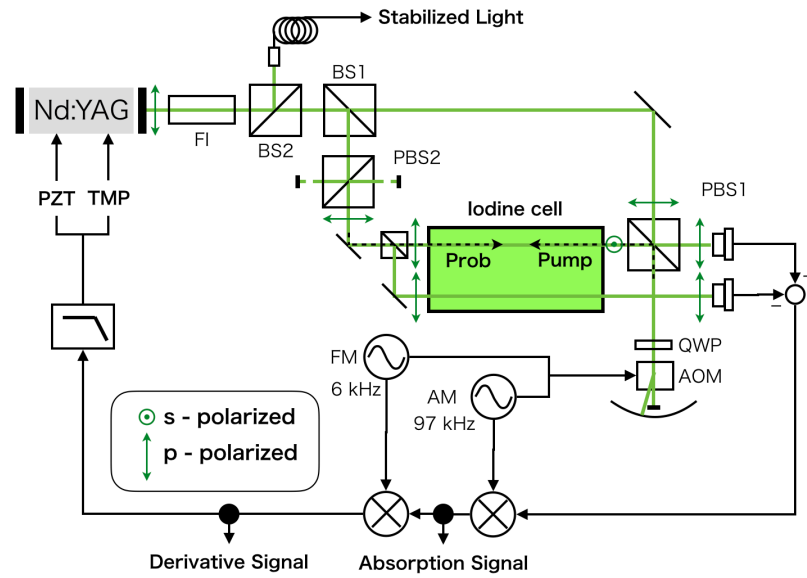


Figure 4.6: Schematic diagram of the frequency-stabilization system of the GIF main laser.

Chapter 5

Baseline Compensation System

5.1 Basics in Seismic Isolation

重力波望遠鏡における地面振動防振の基本は振り子である。より防振比を高めるために、低共振周波数かつ多段振り子をもちいている。

5.1.1 Single Pendulum

For simple example, as shown in left figure in Fig.(5.1), consider a one-dimensional harmonic oscillator consisting of a spring with a spring constant k and mass M . The displacement of the suspension point and the mass are x_0 and x , respectively. Because the equation of the motion is written as

$$M\ddot{x} = -k(x - x_0), \quad (5.1)$$

the frequency transfer function from the displacement of the suspension point to the mass displacement $H(f)$ is given by the Fourier transform from the equation and represented as

$$H(f) \equiv \frac{1}{1 - (f/f_0)^2}, \quad (5.2)$$

where $f_0 = (k/M)^{1/2}$ is the resonant angular frequency of the oscillator.

According to Eq.(5.2), the amplitude of $H(f)$ is unity below the resonant frequency, the amplitude is approximately propotional to $(f/f_0)^{-2}$ above resonance frequency. The bode plot of $H(f)$ with various resonance frequencies

are plotted in right figure in Fig. 5.1 . One finds that it is better to make a low-resonance frequency oscillator in order to attenuate the seismic noise broadly.

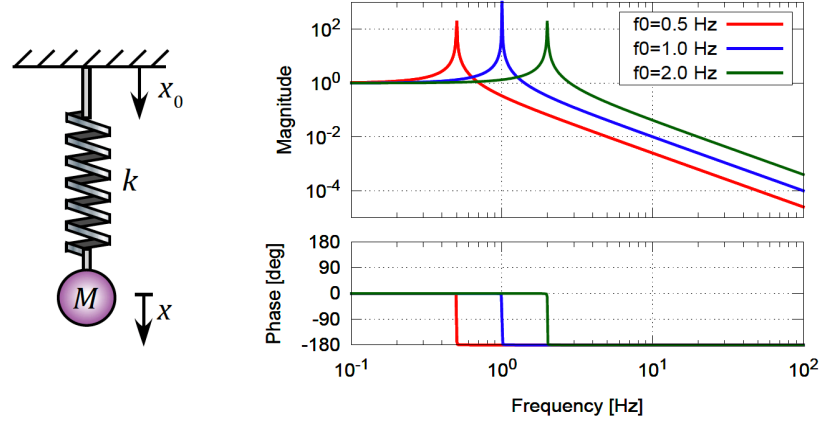


Figure 5.1: Single pendulum as a mechanical filter and its transfer function with various resonant frequencies. This figure is cited from Fig.(2.3) in [29].

5.1.2 Multi-stage Pendulum

In order to increase the order of the seismic isolation, multi-stage pendulum is effective. In case of an N-stage pendulum, the transfer function from the ground to the suspended mass is proportional to f^{-2N} above the resonance frequency of the pendulum as shown in Fig. 5.2.

5.2 Active Inertial Seismic Isolation

振り子をもちいた受動防振ではその共振周波数以下の地面振動は防振できない。さらに低周波で防振するために、広帯域地震計をもちいた能動防振が開発されてきた [30]。

The active isolation system is shown in Fig. 5.3(a). A platform is suspended from the ground with transmissivity H_s . This platform is fed back

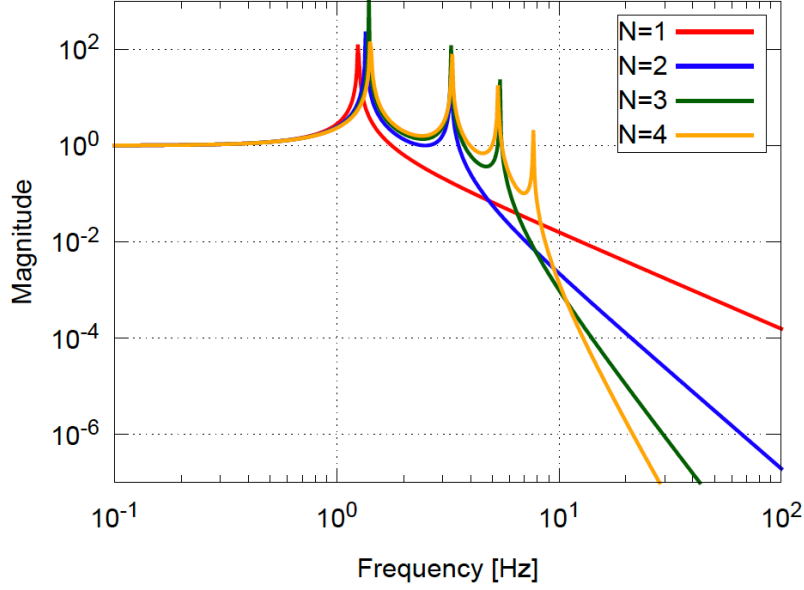


Figure 5.2: The amplitude of the transfer function of the N-stage pendulum. This figure is cited from Fig. 2.4 in [29].

both signal of a inertial sensor with calibration factor S_H and signal of a relative position sensor with calibration factor S_L , to the platform using actuator with actuator efficiency P_a . This feedback control actively decouple the platform from the seismic disturbance from 0.1 Hz to a few Hz. Moreover, the platform is controlled with feedforward using a seismometer with calibration factor S_{wit} installed on the local ground.

能動防振の制御方法は Fig.5.3(b) に示しているとおり、フィードバック制御、センサーコレクション制御、フィードフォワード制御、が組み合わされている。順番にそれらを説明する。

5.2.1 Sensor Blending Technique

Fig.5.4 に示すように、制御信号には慣性センサーと相対位置センサーをブレンドした信号を使う。慣性センサーは低周波で感度が悪くなるので慣性センサーにはハイパスフィルター B_H をかけ、これに対して相対位置センサー

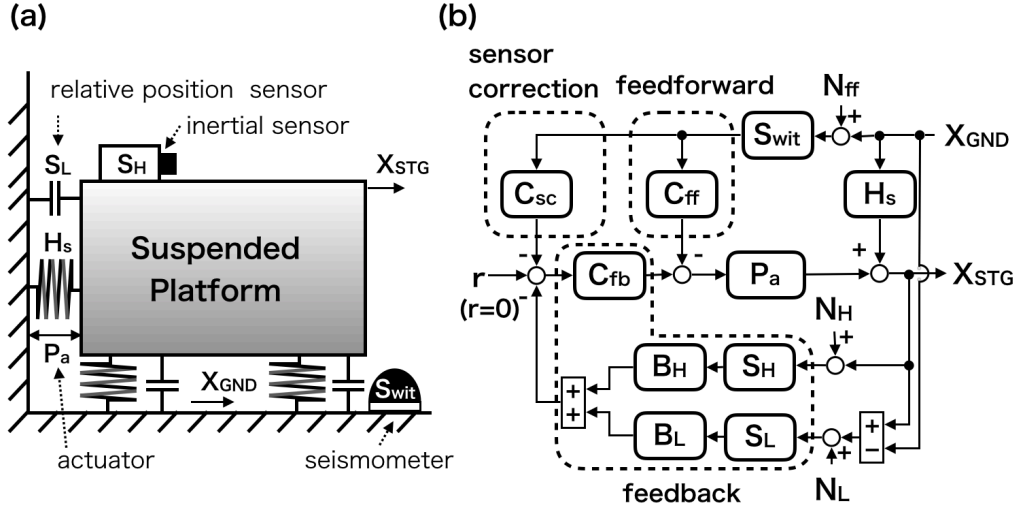


Figure 5.3: (a) Schematic drawing of an active seismic isolation system for platform. (b) Block diagram of the active control scheme.

には、

$$B_H S_H + B_L S_L = 1 \quad (5.3)$$

となるような相補的なローパスフィルター B_L をかける。

このようにブレンドされた制御信号をつかってフィードバック制御した場合での、プラットフォームのステージの変位を考える。まず、platform のステージの変位 X_{STG} は地面振動 X_{GND} 、慣性センサーノイズ N_H 、相対位置センサーのノイズ N_L で表すと

$$X_{STG} = \frac{G}{1+G} L X_{GND} + \frac{1}{1+G} H_s X_{GND} + \frac{G}{1+G} (H N_H + L N_L) \quad (5.4)$$

のようになる。ここで、ループゲインを $G = C_{fb} P_a$ 、相補フィルターとそれぞれのセンサー効率の積を $L = B_H S_H$ 、 $H = B_L S_L$ として、さらに計算の途中で Eq.(5.3) をつかった。すなわち、フィードバック制御が十分に働いている場合、つまりループゲインの値が十分に大きいときのステージの変位は

$$\lim_{G \rightarrow \infty} X_{STG} = L X_{GND} + (H N_H + L N_L) \quad (5.5)$$

である。

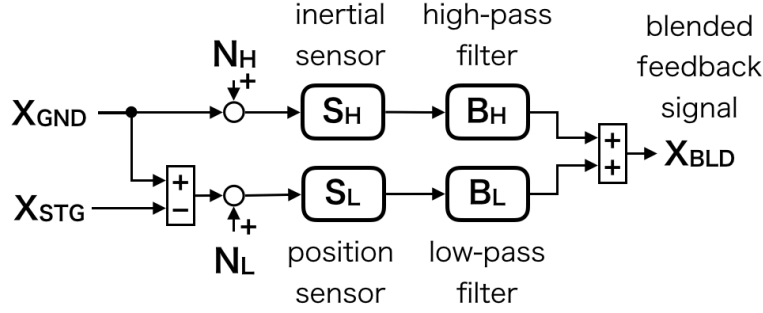


Figure 5.4: Sensor Blending.

Eq.(5.5) によれば、ステージの変位を慣性系に対して防振させるためには伝達関数 L を小さくすればよいが、これは同時に相補フィルターである H を大きくすることを意味し、かえって慣性センサーのノイズをステージに流入させてしまう。現実的には、ローパスフィルター B_L のカットオフ周波数は 100 mHz が限界であり、それ以下の周波数では地面振動は防振されない。別の言い方をすれば、慣性センサーをつかったフィードバック制御は、ブレンディングフィルター L で地面振動からステージへの応答を整えることができる一方で、低周波の感度不足によって防振できる帯域が制限される。

5.2.2 Sensor Correction Technique

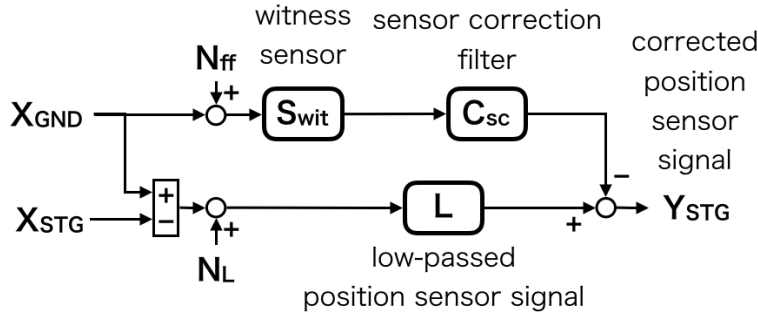


Figure 5.5: Sensor correction scheme.

センサーコレクション制御は相対位置センサーを慣性センサーに修正するための方法である。[31]。上述したとおり、Eq.(5.3) の関係をもつ相補フィルターでブレンドされた制御信号をつかうと、慣性センサーの感度が足りな

い低周波帯域では、相対位置センサーの信号をつかってフィードバック制御をしなければならない。この相対位置センサーは地面からのステージの変位を測るので、低周波帯域では、ステージは地面に対して同じに動くことを意味する。そこで Fig.5.5 に示すように、もう一つ別の地面においた感度の良い地震計で測定した地面振動をつかって、変位センサーの信号から地面振動成分を取り除く。この修正された相対位置センサーの信号を制御信号につかえば、ステージに置いた慣性センサーの感度不足を補うことができる。

センサーコレクションをつかった場合のステージの変位を考える。Fig.5.3 に示すように、センサーコレクションの信号は制御フィルター C_{sc} を経てセットポイントで制御信号から地面振動成分を取り除く。この修正によって、ステージの変位は

$$\begin{aligned} X_{STG} = & \frac{G}{1+G}L \left(1 - C_{sc} \frac{S_{wit}}{L} \right) X_{GND} + \frac{1}{1+G} H_s X_{GND} \\ & + \frac{G}{1+G} (H N_H + L N_L) + \frac{G}{1+G} C_{sc} S_{wit} N_{ff} \end{aligned} \quad (5.6)$$

のように与えられる。フィードバックが働くようにループゲインを十分大きくすると、

$$\lim_{G \rightarrow \infty} X_{STG} = L \Delta_{sc} X_{GND} + (H N_H + L N_L) + L N_{ff} \quad (5.7)$$

になる。ここでゲインマッチ誤差を

$$\Delta_{sc} \equiv \left(1 - C_{sc} \frac{S_{wit}}{L} \right) \quad (5.8)$$

とした。したがって Eq.(5.7) は Eq.(5.5) と比較すると、ステージの変位はゲインマッチ Δ_{sc} によって地面振動の寄与を低減できることがわかる。

このゲインマッチは、Eq.(5.8) によれば $C_{sc} = B_L(S_{wit}/S_L)$ のときゼロになるが、実際は Witness センサーとステージに置いた慣性センサーのキャリブレーションエラーで制限される。現実的にはキャリブレーションエラーはすくなくとも 5%程度になるので、センサーコレクションのみで防振比を 20 以上にするのは難しい [31]。

5.2.3 Feedforward Technique

センサーコレクションに似た方法として feedforward 制御がある。これはステージの地面振動揺れを直接取り除く方法である。Fig.5.6 に示すように、地

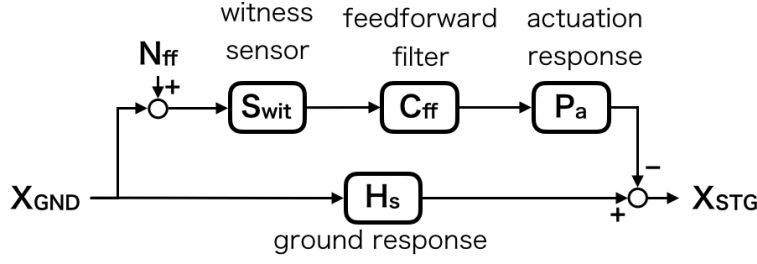


Figure 5.6: Sensor correction scheme.

面からのステージへの伝達関数 H_s で伝わるステージの揺れを、地面においた Witness センサーで測った地面振動の信号をつかってステージを P_s で動かす。このフィードフォワード制御はフィードバック制御に依らない。つまり、フィードフォワード制御はフィードバックループが小さい帯域で働き、一方でセンサーコレクション制御はフィードバックループが大きい帯域ではたらく。このような2つの制御をフィードバック制御に組み合わせることで、地面振動ノイズを低減する。

フィードフォワード制御、センサーコレクション制御、フィードフォワード制御で制御されている状態での、ステージの変位を考える。Fig.5.3 にしめすとおり、エラーポイントにフィードフォワード信号を、セットポイントにセンサーコレクション信号を入れる。このときのステージの変位は、

$$\begin{aligned}
 X_{\text{STG}} = & \frac{G}{1+G} L \Delta_{\text{sc}} X_{\text{GND}} + \frac{1}{1+G} \Delta_{\text{ff}} X_{\text{GND}} \\
 & + \frac{G}{1+G} (H N_H + L N_L) + \frac{G}{1+G} C_{\text{sc}} S_{\text{wit}} N_{\text{ff}} \\
 & + \frac{1}{1+G} P_a C_{\text{ff}} S_{\text{wit}} N_{\text{ff}}
 \end{aligned} \tag{5.9}$$

となる。ここで新たにフィードフォワード制御でのゲインマッチ誤差

$$\Delta_{\text{ff}} \equiv (H_s - P_a C_{\text{ff}} S_{\text{wit}}) \tag{5.10}$$

を導入した。Eq.(5.9)において、地面振動からの寄与を表す第一項と第二項はそれぞれ、ループゲイン G とは独立して、 Δ_{sc} と Δ_{ff} をつかって低減できることがわかる。

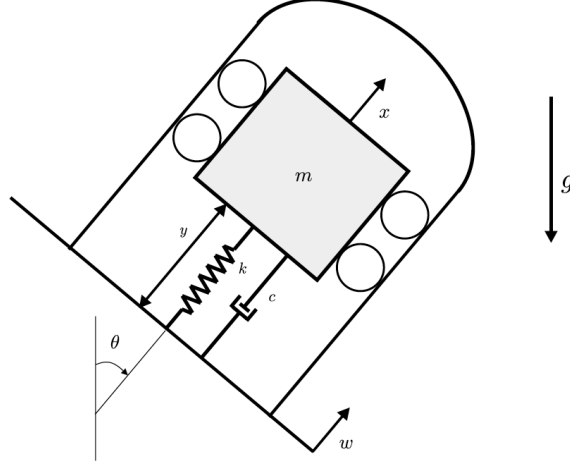


Figure 5.7: Tilted inertial sensor. Cited from Fig.12 in [32]

5.2.4 Problem in Tilt-Horizontal Coupling

慣性センサーは慣性系からみた見かけの力を測るので、地面の加速度運動と傾斜による重力加速度の変化を区別することはできない。これは Tilt-Horizontal カップリングとして知られ、次式のように、センサー信号は地面振動と傾斜の両方に応答してしまう [32]。

$$Y(s) = \frac{-ms^2}{ms^2 + cs + k} \left[W(s) + \frac{g \sin(\theta_0)}{s^2} \Theta(s) \right] \quad (5.11)$$

ここで、 $W(s)$, $Y(s)$, $\Theta(s)$ はそれぞれラプラス空間での、振動子の変位、センサーが測る筐体と振動子との相対変位、筐体の傾斜角である。また m , c , k , g , θ_0 はそれぞれ、振動子の質量、粘性減衰係数、ばね定数、重力加速度、つりあいの状態での角度である。Eq.(5.12) によれば、

$$f < \sqrt{\frac{g \sin(\theta_0)}{(2\pi)^2}} \text{ [Hz]} \quad (5.12)$$

のとき傾斜成分が卓越してくる。たとえば最も傾斜からのカップリングが大きい $\theta_0 = \pi/2$ のとき、つまり地面振動の並進成分は $f < 0.5$ [Hz] のとき傾斜成分に埋もれてしまう。

このように低周波では傾斜計として振る舞う慣性センサーを能動防振につかうことはできない。したがって傾斜成分を別の慣性センサーで測定して、

制御信号から傾斜成分を取り除くことが必要となり制御が複雑になってしまう [33]。

5.3 Suspension Point Interferometer (SPI)

5.3.1 Basic Idea

基線長の能動防振のアイデアは Drever によって 30 年前に考案された。このアイデアは、腕共振器の懸架点間の長さを Suspension point interferometer (SPI) と呼ばれる補助光学系をつかって測り、その信号で懸架点間の距離を一定に保つように制御するというものであった [34]。慣性センサーをもちいた能動防振とは異なり、低周波で感度が良いので、SPI をもちいた能動防振は DC まで防振することができる。これは最大の利点である。

Fabry-Perot Type SPI

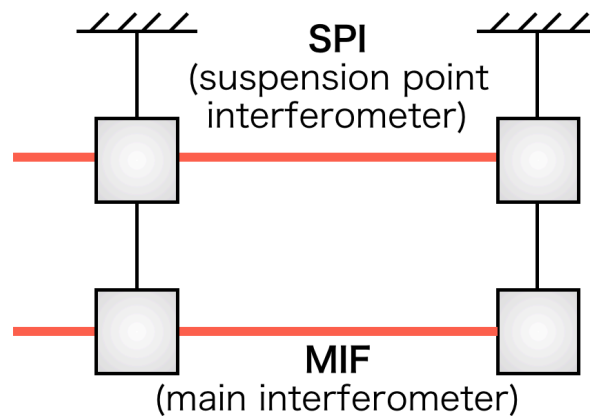


Figure 5.8: Schematic arrangement for one arm of SPI.

当時のアイデアでは SPI にコーナーキューブをエンド鏡に利用した非対称マイケル干渉計をもちいていたが、よりテストマスに近い位置で高精度に基線長を制御するために、Fig.5.8 に示すように、主干渉計と同じく Fabry-Perot 光共振器をつかいフィードバック制御するプロトタイプが提案され [35]、2m の SPI では主干渉計のノイズを 1 Hz 以下で 40 dB 低減することが実証された [36]。

5.3.2 RMS Reduction

SPIをつかえば腕共振器長のRMSを低減することができる。

腕共振器のRMSが小さくなれば後述するとおり、重力波望遠鏡にとってさまざまな利点を与える。

5.3.3 Noise Improvement

Actuator Noise

腕共振器のRMSが小さくなることで、テストマスのアクチュエータ効率を小さくでき、アクチュエータ雑音を小さくすることができる。

Barkhausen Noise

腕共振器のRMSが小さくなることで、アクチュエータにかかる電圧値を小さくでき、バルクハウゼンノイズを低減することが期待できる。

5.3.4 Facilitation of Lock Acquisition

腕共振器のRMSが小さくなることで、ロックアクイジションが容易になる。

5.3.5 Some Difficulties

Difficulty due to Asymmetry of the Suspensions

SPIをつかった能動防振は共振器長さを一定にたもつように制御するので、腕共振の同相の動きは防振できない。このとき、サスペンションの非対称性から同相雑音除去比が悪いと、この同相成分が腕共振器長にカップルしてしまう。

Difficulty in Large Scale GW detectors

SPIの欠点は、建設のコストとアラインメントの難しさにある。

5.4 Baseline Compensation System

5.4.1 Concept

SPIをつかった能動防振の防振性能はCMRRで決まるため、CMRRが悪くなる共振周波数以上の帯域では能動防振をしない。

5.4.2 Advanatge of GIF

5.4.3 GIF as SPI

5.4.4 Control Scheme

5.5 Summary of the Chapter

Chapter 6

Demonstration of Arm Length Compensation Control

6.1 Experimental Arrangement

6.1.1 ...

6.2 Results

6.2.1 ...

6.3 Discussion and Summary of the Chapter

6.3.1 Discussion

6.3.2 Summary

Chapter 7

Conculusion and Future Directions

7.1 Conclusion

7.2 Future Directions

Bibliography

- [1] T Uchiyama, K Furuta, M Ohashi, S Miyoki, O Miyakawa, and Y Saito. Excavation of an underground site for a km-scale laser interferometric gravitational-wave detector. *Classical and Quantum Gravity*, 31(22):224005, 2014. [Link](#).
- [2] Yukio Isozaki, Kazumasa Aoki, Takaaki Nakama, and Shuichi Yanai. New insight into a subduction-related orogen: a reappraisal of the geotectonic framework and evolution of the japanese islands. *Gondwana Research*, 18(1):82–105, 2010. [Link](#).
- [3] T Akutsu and et. al. Construction of kagra: an underground gravitational-wave observatory. *Progress of Theoretical and Experimental Physics*, 2018(1), 01 2018. [Link](#).
- [4] Yoichi Aso, Yuta Michimura, Kentaro Somiya, Masaki Ando, Osamu Miyakawa, Takanori Sekiguchi, Daisuke Tatsumi, and Hiroaki Yamamoto. Interferometer design of the kagra gravitational wave detector. *PHYSICAL REVIEW D Phys Rev D*, 88:043007, 2013. [Link](#).
- [5] Kentaro Somiya. Detector configuration of kagra the japanese cryogenic gravitational-wave detector. *Classical and Quantum Gravity*, 29(12):124007, jun 2012. [Link](#).
- [6] Okutomi Koki. *Development of 13.5-meter-tall Vibration Isolation System for the Main Mirrors in KAGRA*. PhD thesis, SOKENDAI, The Graduate University for Advanced Studies, 2019. [Link](#).
- [7] Shuichi Sato, Shinji Miyoki, Souichi Telada, Daisuke Tatsumi, Akito Araya, Masatake Ohashi, Yoji Totsuka, Mitsuhiro Fukushima, Masa-

- Katsu Fujimoto, LISM Collaboration, et al. Ultrastable performance of an underground-based laser interferometer observatory for gravitational waves. *Physical Review D*, 69(10):102005, 2004.
- [8] M Punturo, M Abernathy, F Acernese, B Allen, Nils Andersson, K Arun, F Barone, B Barr, M Barsuglia, M Beker, et al. The einstein telescope: a third-generation gravitational wave observatory. *Classical and Quantum Gravity*, 27(19):194002, 2010.
- [9] B P Abbott, R Abbott, T D Abbott, M R Abernathy, K Ackley, C Adams, P Addesso, R X Adhikari, V B Adya, C Affeldt, et al. Exploring the sensitivity of next generation gravitational wave detectors. *Class. Quantum Grav*, 34(044001):044001, 2017.
- [10] L Naticchioni, M Perciballi, F Ricci, E Coccia, V Malvezzi, F Acernese, F Barone, G Giordano, R Romano, M Punturo, et al. Microseismic studies of an underground site for a new interferometric gravitational wave detector. *Classical and Quantum Gravity*, 31(10):105016, 2014.
- [11] 竹本修三, 新谷昌人, 赤松純平, 森井互, 東敏博, 福田洋一, 尾上謙介, 市川信夫, 川崎一朗, 大橋正健, et al. 神岡鉱山における 100 メートルレーザー伸縮計について. 2003.
- [12] Sylvette Bonnefoy-Claudet, Fabrice Cotton, and Pierre-Yves Bard. The nature of noise wavefield and its applications for site effects studies: A literature review. *Earth-Science Reviews*, 79(3-4):205–227, 2006.
- [13]
- [14] M G Beker, J F J van den Brand, E Hennes, and D S Rabeling. Newtonian noise and ambient ground motion for gravitational wave detectors. *Journal of Physics: Conference Series*, 363:012004, jun 2012.
- [15] R. Schofield et al. Source and propagation of the predominant 1-50 hz seismic signal from off-site at ligo-hanford. In LIGO Scientific Collaboration Meeting, Hanford, August 2000.

- [16] F Acernese, P Amico, N Arnaud, D Babusci, R Barillé, F Barone, L Barsotti, M Barsuglia, F Beauville, MA Bizouard, et al. Properties of seismic noise at the virgo site. *Classical and Quantum Gravity*, 21(5):S433, 2004.
- [17] Jon R Peterson. Observations and modeling of seismic background noise. Technical report, US Geological Survey, 1993.
- [18] Kiwamu Nishida, Naoki Kobayashi, and Yoshio Fukao. Origin of earth’s ground noise from 2 to 20 mhz. *Geophysical Research Letters*, 29(10):52–1, 2002.
- [19] P Bormann. New manual of seismological observatory practice. *GFZ German Research Centre for Geosciences*, 2012. [Link](#).
- [20] RA Haubrich, WH Munk, and FE Snodgrass. Comparative spectra of microseisms and swell. *Bulletin of the Seismological Society of America*, 53(1):27–37, 1963. [Link](#).
- [21] Michael Selwyn Longuet-Higgins. A theory of the origin of microseisms. *Philosophical Transactions of the Royal Society of London. Series A, Mathematical and Physical Sciences*, 243(857):1–35, 1950. [Link](#).
- [22] GG Sorrells, John A McDonald, ZA Der, and Eugene Herrin. Earth motion caused by local atmospheric pressure changes. *Geophysical Journal International*, 26(1-4):83–98, 1971.
- [23] W Zürn and R Widmer. On noise reduction in vertical seismic records below 2 mhz using local barometric pressure. *Geophysical Research Letters*, 22(24):3537–3540, 1995.
- [24] A ARAYA. Broadband observation with laser strainmeters and a strategy for high resolution long-term strain observation based on quantum standard. *J. Geod. Soc. Japan*, 53:81–97, 2007.
- [25] Nanometrics Inc., 250 Herzberg Road Kanata, Ontario, Canada K2K 2A1. *Trillium 120Q/QA User Guide*, 04 2017.

- [26] Rolf Bork, R Abbott, D Barker, and J Heefner. An overview of the ligo control and data acquisition system. *arXiv preprint physics/0111077*, 2001.
- [27] Norman Bobroff. Recent advances in displacement measuring interferometry. *Measurement Science and Technology*, 4(9):907, 1993.
- [28] Mark A Zumberge, Jonathan Berger, Matthew A Dzieciuch, and Robert L Parker. Resolving quadrature fringes in real time. *Applied optics*, 43(4):771–775, 2004.
- [29] Takanori Sekiguchi. *A Study of Low Frequency Vibration Isolation System for Large Scale Gravitational Wave Detectors*. PhD thesis, Department of Physics School of Science, University of Tokyo, 2016.
- [30] F Matichard, B Lantz, R Mittleman, K Mason, J Kissel, B Abbott, S Biscans, J McIver, R Abbott, S Abbott, et al. Seismic isolation of advanced ligo: Review of strategy, instrumentation and performance. *Classical and Quantum Gravity*, 32(18):185003, 2015.
- [31] Wensheng Hua. *LOW FREQUENCY VIBRATION ISOLATION AND ALIGNMENT SYSTEM FOR ADVANCED LIGO*. PhD thesis, stanford university, 2005.
- [32] Christophe Collette, Stefan Janssens, Pablo Fernandez-Carmona, Kurt Artoos, Michael Guinchard, Claude Hauviller, and André Preumont. Inertial sensors for low-frequency seismic vibration measurement. *Bulletin of the seismological society of America*, 102(4):1289–1300, 2012.
- [33] Sebastien Biscans. Optimization of the advanced ligo gravitational-wave detectors duty cycle by reduction of parametric instabilities and environmental impacts.
- [34] Outline of a proposed design for a first receiver for installation in the long-baseline facilities, of fabry-perot type. Technical report.
- [35] Ronald WP Drever and Steven J Augst. Extension of gravity-wave interferometer operation to low frequencies. *Classical and Quantum Gravity*, 19(7):2005, 2002.

- [36] Y Aso, M Ando, K Kawabe, S Otsuka, and K Tsubono. Stabilization of a fabry–perot interferometer using a suspension-point interferometer. *Physics Letters A*, 327(1):1–8, 2004.